Keywords: Rydberg atoms; Nonlinear dynamics **PACS:** 32.80.Ee, 47.20.Ky, 05.45.-a

Continuous time quasi-crystal and its transition to continuous time crystal in coupled Rydberg atomic chains

Weilun Jiang[1, *]

[1] *State Key Laboratory of Quantum Optics Technologies and Devices, Institute of Opto-Electronics, Collaborative Innovation Center of Extreme Optics, Shanxi University, Taiyuan, 030006, China*

(Dated: August 21, 2026)

We investigate the nonlinear dynamics of two coupled driven–dissipative Rydberg atomic chains, each of which formed a previously reported continuous time crystal phase. By tuning the inter-chain interaction, the two time-crystalline subsystems with distinct intrinsic oscillation frequencies will naturally mix, and support luxuriant stable and collective oscillatory behavior. We identify a dynamical phase characterized by quasi-periodic oscillations with multiple incommensurate frequencies, corresponding to a continuous-time quasi-crystalline order. In addition, we identify a phase transition from a time quasi-crystalline phase to a time-crystalline phase at sufficiently strong inter-chain coupling. This transition can be understood as the evolution from partially synchronized oscillations between the two chains to fully synchronized dynamics. From a mathematical perspective, we confirm that the transition is governed by either a saddle-node or a torus bifurcation, depending on the separation between the two original oscillation frequencies. These theoretical results provide guidance for exploring complex periodic dynamics in Rydberg atomic platforms.

I. INTRODUCTION

Rydberg atomic systems have emerged as a versatile platform for exploring non-equilibrium many-body physics due to their strong and controllable interactions [1–26]. In particular, the long-range interactions between Rydberg excitations give rise to strong nonlinearities. In the presence of spontaneous decay of the Rydberg states and continuous pumping from the ground state, the system forms a driven–dissipative platform in which such nonlinear effects could lead to the emergence of a non-equilibrium phase - continuous time crystal (CTC) [27–32]. Considering a system with a large number of atoms, its dynamics can often be captured within a mean-field (MF) framework, where the emergence of stable oscillations corresponds to limit cycle solutions of the nonlinear dynamical equations. A crucial ingredient for these oscillatory phases is nonlinearity, since purely linear systems cannot sustain stable periodic solutions [33]. In Rydberg systems, the required nonlinearity can arise from mechanisms such as competition between Rydberg levels [34] or higher-order terms induced by the higher Rydberg population [35, 36]. More generally, the interplay between nonlinear interactions and dissipation in open systems provides a powerful route for stabilizing time-crystalline order and other non-equilibrium phases.

Beyond conventional CTCs, an intriguing extension is the concept of a continuous time quasi-crystal (CTQC), characterized by multiple incommensurate oscillation frequencies and their combination in the Fourier spectrum [37–41]. Such phases have not yet been observed on Rydberg atomic systems, raising the question of how they may be engineered. A possible mechanism may be naturally proposed, based on coupling two continuous time crystalline subsystems with distinct intrinsic oscillation frequencies. Under such a design, their collective dynamics may produce multiple internal oscillation modes, providing a natural route toward realizing time quasi-crystalline order. This approach has already been successfully demonstrated in the generation of discrete time quasi-crystals in various systems [42–44].

However, a key challenge is that generic coupling between oscillatory subsystems often leads to dynamical instabilities or chaotic behavior rather than stable quasi-periodic motion [39]. To overcome this difficulty, we employ the same nonlinear interaction underlying time crystal formation in Rydberg atoms to couple the two CTCs - the density-density interaction. By employing tunable interaction parameters, this scheme allows controlled coupling of the two subsystems while ensuring that the system does not reach a state of chaos. Importantly, the proposed setup can be implemented with Rydberg atomic platforms.

In this theoretical work, we investigate a system consisting of two coupled Rydberg atomic chains and analyze its nonlinear MF dynamics. Our results reveal the existence of a robust time quasi-crystalline phase characterized by aperiodic oscillations in the time domain, and a Fourier spectrum composed of multiple sharp and incommensurate peaks. By mapping out the phase diagram, we identify the phase region where two distinct CTQC phases coexist, as well as the region where CTC and CTQC orders appear simultaneously. The associated phase transitions can be interpreted as torus bifurcations in nonlinear dynamical systems. Near the transition points, we further perform a quantitative analysis and show that the difference between the dominant frequency components of two subsystems follows a square-root scaling with respect to the tuning parameters. These results provide a concrete theoretical pathway for realizing and controlling time quasi-crystalline phases in Rydberg systems and open new directions for exploring complex non-equilibrium orders in strongly interacting atomic platforms.

* wljiang@sxu.edu.cn

II. MODEL HAMILTONIAN AND MEAN-FIELD APPROACH

We consider two coupled Rydberg atomic chains as shown in Fig. 1(a). The distance between the two chains is an essential tunable parameter in our model, which determines the interaction between two chains. The total Hamiltonian contains three parts,

$$\begin{aligned} H &= H_1 + H_2 + V_{\text{int}} \\ &= \sum_i (\frac{\Omega_1}{2}\sigma_{1i}^x - \Delta_1 n_{1i}) + V\sum_{\langle i,j\rangle} n_{1i}n_{1j} \\ &+ \sum_i (\frac{\Omega_2}{2}\sigma_{2i}^x - \Delta_2 n_{2i}) + V\sum_{\langle i,j\rangle} n_{2i}n_{2j} + V_{\text{int}}, \end{aligned} \tag{1}$$

where the two chains are labeled 1 and 2 and the atomic sites are labeled i. The intra-chain nearest-neighbor (NN) interaction strength is V, and all the inter-chain interaction terms are included in V_{int}. In particular, the NN interaction is denoted as V_i, and next nearest-neighbor (NNN) interaction V_{i2}. The whole terms writes,

$$V_{\text{int}} = V_i \sum_i n_{1i}n_{2i} + V_{i2}\sum_{\langle i,j\rangle}(n_{1i}n_{2j} + n_{2i}n_{1j}) + \cdots, \tag{2}$$

where the ellipsis encompasses long-range inter-chain interactions. Within the Rydberg blockade radius, the Rydberg interaction strength decays as $\sim \frac{1}{d^6}$, where d is the distance between two atoms. Therefore, the NNN interaction, for example V_{i2} is tiny compared to V and V_i. To simplify computational complexity, we omit V_{i2} and other long-range interactions in most calculations, unless we give a special explanation.

Next, we also introduce the spontaneous emission of the Rydberg level, denoted as γ. The dynamic of the system is described by the Lindblad Master equation,

$$\begin{aligned} \dot{\rho} &= -i\,[H,\rho] + \mathcal{L}(\rho) \\ \mathcal{L}(\rho) &= \gamma\sum_I \left(\sigma_I^- \rho \sigma_I^+ - \frac{1}{2}\{n_I,\rho\}\right). \end{aligned} \tag{3}$$

Here, the summation of I includes all the lattice sites. The dynamics of the full density matrix is always unsolvable at large system sizes. We thus employ the MF approximation in the initial processing. In general, one would assign $\rho(t) = \rho_1(t)\otimes\rho_2(t)\otimes\cdots\otimes\rho_N(t)$ where N is the system size, and expect that at the late time, the solution of each blocked density matrix is the same, i.e. $\rho_{\text{MF}}(t) \equiv \rho_i(t), i = 1, 2, \cdots, N$. The above treatment is based on the stability of the uniform solution. However, previous results show that the antiferromagnetic type perturbation could lead to instability of the uniform solution [45]. Therefore, the proper division of the full density matrix is $\rho(t) = \rho_{1,2}(t)\otimes\rho_{3,4}(t)\otimes\cdots\otimes\rho_{N-1,N}(t)$ (suppose N is an even number), and $\rho_{\text{MF}}(t) \equiv \rho_{i,i+1}(t)$. Extended to the two coupled chains, the repetitive unit of the density matrix involves four sites, as shown in the red region in Fig. 1(a). We write them as $1A, 1B, 2A, 2B$, where A, B are the two

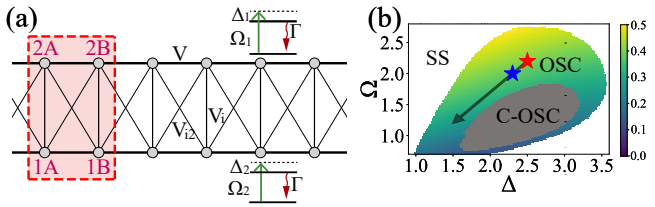


FIG. 1. (a) The sketch map of the model. The atomic site are represented by the grey dots, controlled by uniform Rabi frequency and detuning. The intra-chain NN interaction strength V, the inter-chain NN interaction strength V_i and the NNN interaction strength V_{i2} are denoted by thick, medium-thick, and thin solid lines, respectively. The region solved by MF approach is colored by red. (b) Single chain MF phase diagram. The parameter points (Ω, Δ) of two chains is assigned to be inside the colored region, where the color is associated with the oscillatory frequency. The red (blue) star corresponds to chain 1(2) parameter points, and the arrow represents the movement away trajectory of the parameter point (Ω_2, Δ_2).

NN sites. In particular, we focus on the single site operator, the Rydberg population $|r_I\rangle\langle r_I|$ and the transition amplitude $|r_I\rangle\langle g_I|$, where $|r_I\rangle$ and $|g_I\rangle$ are the basis of the Rydberg state and the ground state on site I, respectively. Substituting into Eq.(3), we get the equation of motion (EOM) of the system, comprised of eight variables n_I and σ_I (see supplementary material for the detailed derivation). Here, n_I and σ_I represent the average value of the Rydberg population and the transition amplitude. In the following text, we will numerically solve the master equation and directly show the dynamics of the CTQC and its transition.

Regarding parameter choice, by design, each chain should form a CTC under MF approximation. According to Ref. [45], we reproduce the single chain phase diagram in Fig. 1(b) at $V = 5$ and $\gamma = 1$. We then choose two parameter points inside the oscillatory solution region, that is $\Omega_1 = 2.2, \Delta_1 = 2.5$ for chain 1 (red star), and $\Omega_2 = 2.0, \Delta_2 = 2.3$ for chain 2 (blue star). Specifically, we calculate the frequency inside the oscillation region, indicated by the colormap. It shows the monotonous variation within the phase, ignoring the gray region where the oscillatory pattern inside is complicated and deviates from the form of a sinusoidal waves.

III. CONTINUOUS TIME QUASI-CRYSTAL PHASE

Continuous time crystal phases have been theoretically demonstrated by the limit cycle solution of the nonlinear EOM of a single chain [45]. For the system of two coupled chains, under the same parameter choices $\Omega_1 = \Omega_2, \Delta_1 = \Delta_2$, two co-existing CTC modes are formed [46]. Such a phase is represented by the occurrence of the two limit cycles. Each limit cycle corresponds to one stable periodic oscillation on the time-dependent solution of EOM. According to their dynamics, the oscillatory pattern where $n_{1\text{A}}(t) = n_{2\text{B}}(t)$ and $n_{1\text{B}}(t) = n_{2\text{A}}(t)$ at all times are identified as the usual two dimensional antiferromagnetic-type oscillation (2DAF) [45]. Regarding the Rydberg density as the magnetic moment

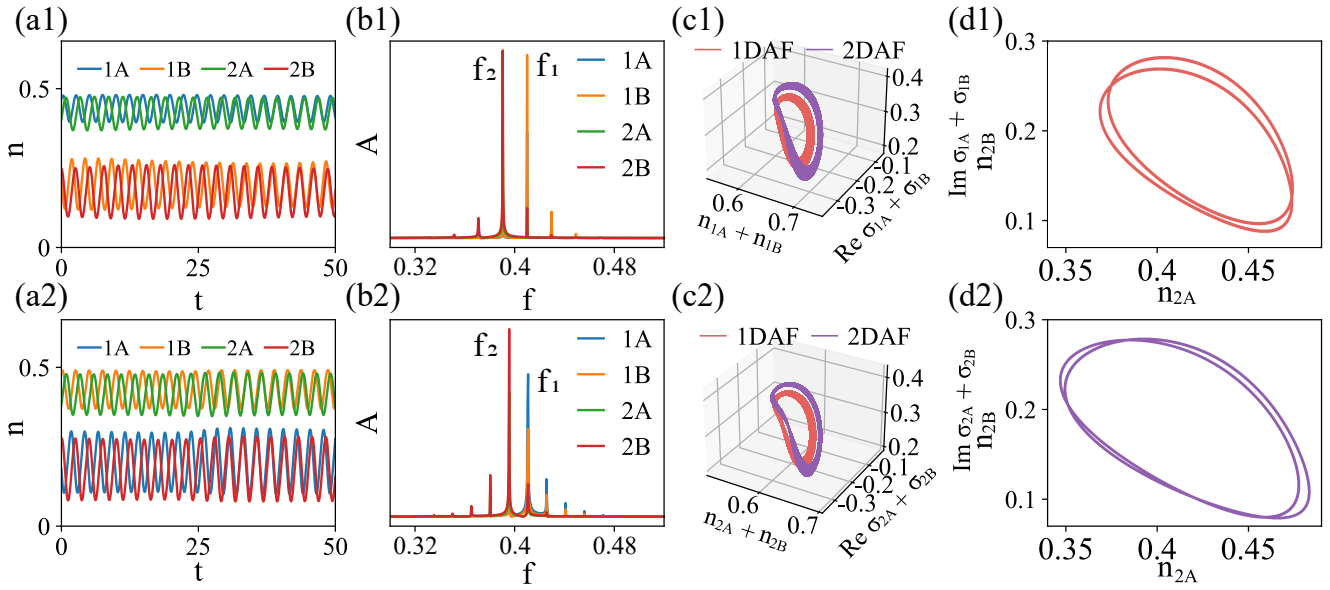


FIG. 2. CTQC phase properties of two modes with $V_i = 0.5$. (a1, b1) Time-dependent solutions of Rydberg population on different sites and associated Fourier spectrums of 1DAF mode. (a2, b2) Time-dependent solutions and associated Fourier spectrums of 2DAF mode. For 1DAF mode in CTQC phase, the time average of n_{1A} is approximately equal to n_{2A}, instead the strictly equal relationship for CTC phase. This also applies to 2DAF mode, where n_{1A} is only approximately equal to n_{2B}. The Fourier spectrums show equidistant peaks, where the dominant frequencies at $f_1 = 0.205$, $f_2 = 0.195$ for (b1), and $f_1 = 0.205$, $f_2 = 0.198$ for (b2). (c1, c2) Three-dimensional phase space trajectory with respect to observables of chain 1 and variable of chain 2. The two modes both show torus structure. (d1, d2) Poincaré section diagram for two oscillatory modes 1DAF and 2DAF, respectively. The scatter points are the crossing points between the trajectory of n_{1A} and its time averaged value. The results are further projected on two-dimensional plane (n_{2A}, n_{2B}) for drawing. Both two figures shows the closed curves. The total simulation time is 10^5, with a time step of $dt = 0.01$. For the discrete Fourier transform, only the latter half of the simulation data is used to exclude transient dynamics. The same procedure is adopted in the following analysis.

along z-axis, the instantaneous configuration resembles a two-dimensional staggered antiferromagnetic arrangement. The other mode satisfies that the time-average value of n_{1A} is equal to n_{2A} (the same as n_{1B} and n_{2B}) is denoted as 1DAF. Next, we will separately calculate the dynamic behaviors of the two oscillatory modes, extended to the quasi-periodic regime.

When considering different parameters of two chains, we find that the peak value within each oscillatory period becomes time-dependent, as shown by the solution of the Rydberg population of each site [Fig. 2(a)]. That means that another oscillatory mode with longer wavelength is superimposed on the original oscillatory pattern. To clearly show this, we display the associated Fourier spectrum of the Rydberg population on each site [Fig. 2(b)]. First, we define the frequency components that have the local maximum amplitude as the major frequencies for each site. All major frequencies for the four sites perfectly coincide, indicating a common oscillatory mode. Moreover, we find that all major Fourier components can be formulated as a linear combination of two frequencies f_1 and f_2, respectively,

$$f = m \times f_1 + n \times f_2, \quad m, n \in \mathcal{Z}. \tag{4}$$

To find its physical counterpart, we could define the dominant frequency for each site $f_{1A}, f_{1B}, f_{2A}, f_{2B}$, where the associated amplitude of the Fourier component is the largest, except for the $f = 0$ points. Moreover, we find that in this case $f_{1A} = f_{1B}$, and $f_{2A} = f_{2B}$, indicating that the dominant frequency of each lattice point on every chain is equal. Therefore, for brevity, we can always consider f_1 and f_2 to be the collective oscillatory dynamics of chains 1 and 2, respectively. This applies to the case at inter-chain interaction $V_i = 0$, where each chain has only one major frequency (also dominant), i.e. $f_1 = 0.40$ and $f_2 = 0.38$. For $V_i \neq 0$, we find that f_1 and f_2 will change along with V_i (see the following discussion), and f_1 and f_2 are always incommensurate. The oscillatory pattern comprised of two incommensurate frequencies is the signal of CTQC in our model. Moreover, it is worth noting that at different initial conditions, the late time solution will flow to two entirely different quasi-periodic oscillation patterns, signaling the two co-existing CTQC at fixed parameters.

To give further confirmation of the CTQC phase, we also demonstrate its trajectory in a three-dimensional phase space [Fig. 2(c)]. Note that the two trajectories colored by represent the two co-existing quasi-periodic oscillations. In both the phase space with respect to chain 1 and chain 2, the trajectories show the two-dimensional structure, known as the torus, rather than the limit cycle structure associated with the CTC. In addition, the Poincaré section analysis [Fig. 2(d)] manifests the closed curve, distinguishing it from the finite number of discrete points (periodic oscillatory), and the infinite number of irregular points (chaotic).

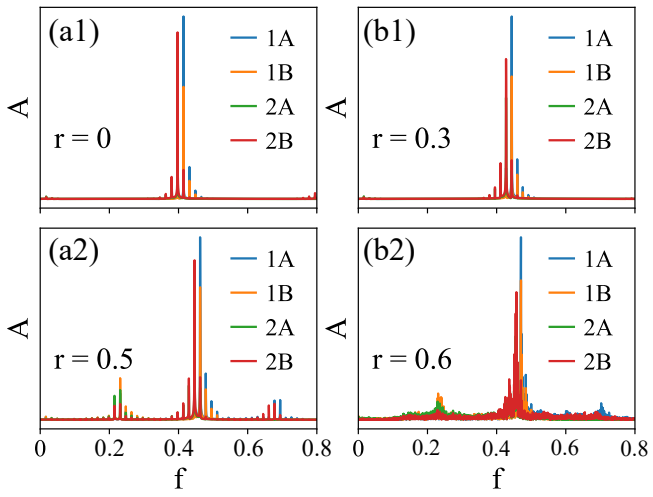


FIG. 3. Fourier spectrum at various non-linearity parameter r at $V_i = 0.5$. Note in this calculation, we also consider the long-range term described by V_{i2}. As r increases, the discrete and clear peaks, signaling the CTQC phase, gradually goes blurry.

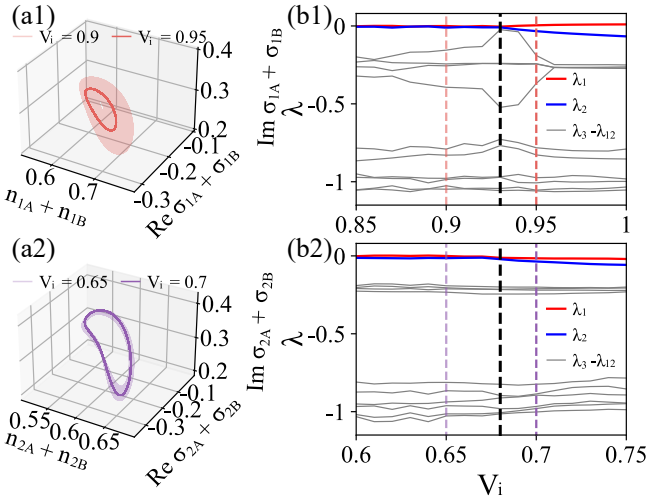


FIG. 4. (a1, a2) Three-dimensional phase space trajectory of two oscillatory mode at two V_i points. The smaller V_i is located in CTQC phase, and the larger one in CTC phase. Both cases show a transition from the torus structure to the limit cycle. (b1, b2) Lyapunov exponent of two oscillatory mode as a function of V_i. The curves of largest eigenvalues are colored and named with λ_1 and λ_2, and others eigenvalues λ_3 to λ_{12} are plotted with thin grey line. The thick black line are putative transition point versus V_i, where λ_2 begin to deviate from zero within the errorbar. The thin colored lines corresponds to the parameter choice for two phase in (a). The transition point is $V_{i,c} = 0.68$ for 1DAF mode, and 0.93 for 2DAF mode.

At the end of this section, we also discuss its robustness of the quasi-periodic oscillation against the MF approximation. As an example, here we include the long-range interaction by setting a finite value to V_2 according to the $\frac{1}{d^6}$ decay, where d is the distance between two Rydberg atoms. Moreover, we take into account high-order expansion of the commutator, and add an extra term $n^2\sigma$ to EOM (see supplementary material for the details). Here, r measures the magnitude of the higher-order nonlinear effect beyond the conventional mean-field contribution, which has been introduced in [47]. Under this condition, we show the Fourier spectrum of the Rydberg population for different r in Fig. 3. As r increases, at $r \lesssim 0.5$, the peaks of each Fourier component remain sharp and clear. The main peaks fulfill the expression in Eq. (4). However, at large r, the signals of other frequencies have a non-negligible amplitude, and the dynamic finally goes chaotic. We thus conclude that at small non-linearity, the CTQC behavior is stable. In fact, CTQC exists as a considerable phase in the entire parameter space. In the following text, we will conduct a detailed analysis of the phase diagram and properties of the transition.

IV. TRANSITION TO CONTINUOUS TIME CRYSTAL PHASE

In our model, CTQC behavior originates from the CTC phase, due to the different frequencies of the two coupled system, where the inter-chain coupling strength V_i plays an important role in tuning the transition from the CTQC to the CTC phase. Furthermore, CTQC is regarded as the mixture of two systems that are not fully synchronized, since the dominant frequencies of two chains are different, i.e., $f_1 \neq f_2$. While the CTC, where the two chains oscillate at only one dominant frequency, stands for that the difference of two inherent frequencies is eliminated by the coupling. Hence, one would generally expect that CTC may occur at large V_i, and that CTQC exists when the coupling strength is sufficiently small. Numerically, we verify the transition by three approaches: the phase space trajectory, Lyapunov exponent, accompanied by Fourier spectrum analysis.

Fig. 4 shows the numerical results of the first two approaches at different V_i points. Note we still separately discuss the with respect to two synchronized modes, thus different initial states are chosen to distinguish two results. When V_i increases, the phase space trajectories transfer from the torus to the limit cycle [Fig. 4(a)]. Meanwhile, the largest two Lyapunov exponents convert from both zero to a non-zero [Fig. 4(b)]. Specifically, the case where only one Lyapunov exponent is zero and the others are all negative corresponds to the limit cycle solution. when there are two zero Lyapunov exponents, the dynamics exhibits two oscillations in the vertical direction, in accordance with the torus. It follows that the above two analyzes give consistent critical points. Mathematically, the transition points are identified as the saddle-node bifurcation points, which emerge in our model with respect to the coupling strength.

We proceed to explore the variance of the main frequencies passing the transition point in Fig. 5, taking 1DAF mode as an example. Toward the transition point from the CTQC phase, the two dominant frequencies gradually get closer to each other. Regarding other sum frequencies and difference frequencies, the amplitudes monotonically decrease as the fre-

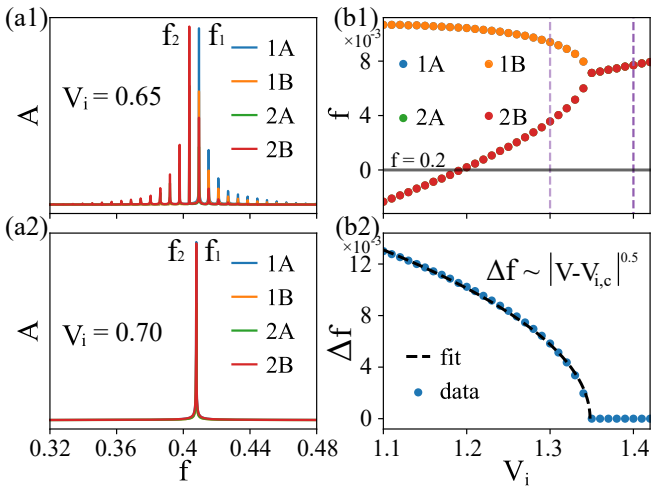


FIG. 5. (a1, a2) Fourier spectrum in CTQC and CTC phase of 1DAF mode. In CTQC phase, the amplitude of two chains seems to be symmetric near transition point. (b1) The extracted dominant frequency of different sites as a function of V_i. Note that $f_{1A} = f_{2A}$, and $f_{1B} = f_{2B}$. The two dominant frequencies of two chains change from inequality to equivalence. The colored dashed lines represent the parameter choice for two phase in (a). Note that all dominant frequency are very close 0.2. (b2) The two chains frequency difference Δf as a function of V_i. We fit data points with the function form $\Delta f = c|V_i - V_{i,c}|^{\alpha}$, and get $\alpha = 0.50, c = 0.0186, V_{i,c} = 0.674$.

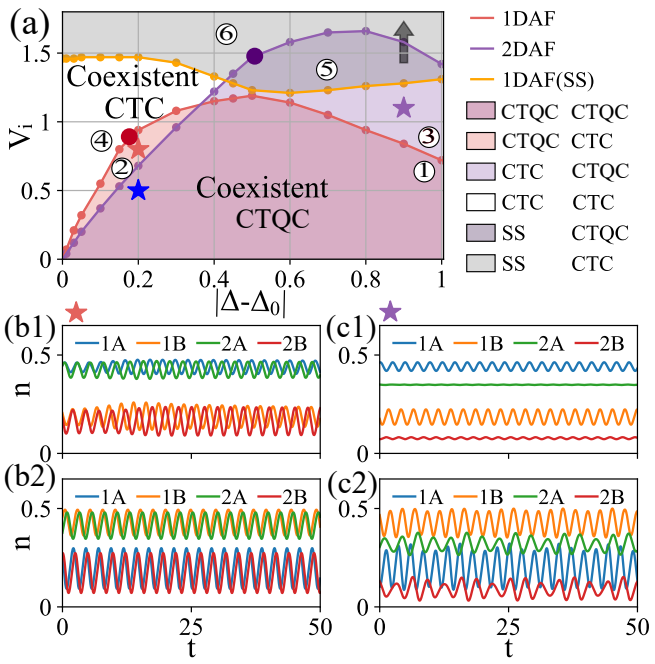


FIG. 6. (a) The phase diagram with respect to the parameter difference and inter-chain strength. The data are obtained by fixed $|\Delta - \Delta_0|$ and scanning V_i, with associated error smaller than 0.01. Three boundaries divide the parameter space into six distinct regions. For the phase region legends, the first (second) column represents the phase of 1DAF (2DAF) mode. The blue points is the parameter points that was previously explored. The critical points Δ_c distinguishing saddle-node and torus bifurcations, are marked on the transition boundary. (b1, b2) The Rydberg population dynamics at red stars for 1DAF and 2DAF mode, respectively. It shows the CTQC behavior for 1DAF mode, and CTC behavior for 2DAF mode. (c1, c2) The Rydberg population dynamics at purple stars for 1DAF and 2DAF mode, respectively. It shows the CTC behavior for 1DAF mode, and CTQC behavior for 2DAF mode. Compared with the CTC phase with same two-chain parameters [46], the phase of periodical oscillation is not exactly locked to π (1DAF mode) or 0 (2DAF mode).

quency components go away from the dominant frequency. In addition, the Fourier spectrum of chain 1 and chain 2 gradually turns into symmetric with respect to the frequency at the transition point, and its summation becomes more like an even function [Fig. 5(a)].

To quantitatively determine the transition point between CTQC and CTC, we first introduce a criterion for the transition point between CTQC and CTC as $V_{i,c,amp}$, based on the spectrum amplitude. At $V \geq V_{i,c}$, there is only one main frequency existing (except for the harmonics). Such a criterion fully captures the CTC character, that only single frequency dominants. Numerically, we have $V_{i,c} = 0.673$ (not shown here). The second approach is by definition of the frequency difference $\Delta f \equiv |f_1 - f_2|$. We fit Δf with respect to the distance to the transition point $V_i - V_{i,c}$ in the CTQC phase by a power law function form [Fig. 5(b)]. Here, $V_{i,c}$ serves as a fitting parameter, and we obtain $V_{i,c,\text{fit}} = 0.674$, which is almost the same as $V_{i,c}$. In addition, the fitting result is close to that of the Lyapunov exponent criterion in Fig. 4(b2). This indicates that the results of the different methods are highly consistent.

Importantly, we find the frequency relation from the above fitting,

$$\Delta f \sim \sqrt{V_i - V_{i,c}} \tag{5}$$

which quantitatively reveals the frequency changes near the transition point. Such critical behavior further indicates the transition belongs to the saddle-node bifurcation. It occurs when a stable and an unstable fixed point collide and annihilate, giving rise to a square-root scaling law near the transition point.

V. PHASE DIAGRAM

In this section, we no longer fix the parameters of two chains. Instead, we introduce the distance between two parameter sets defined in the parameter space (Ω, Δ) as shown in Fig. 1(b). For brevity, we fix (Ω_1, Δ_1) as one end of the line segment (red star), and (Ω_2, Δ_2) is the mobile point on the arrow (blue star). Subsequently, we use $|\Delta_2 - \Delta_1|$ to characterize the distance between two parameter points. At first glance, the larger the initial frequency difference, the greater the interaction strength required for the two chains to reach synchronization. However, we numerically find the complex phase diagram, including both CTQC and CTC phases, and the non-monotonic behavior evolution [Fig. 6(a)].

As in the previous text, we separately calculate the phase

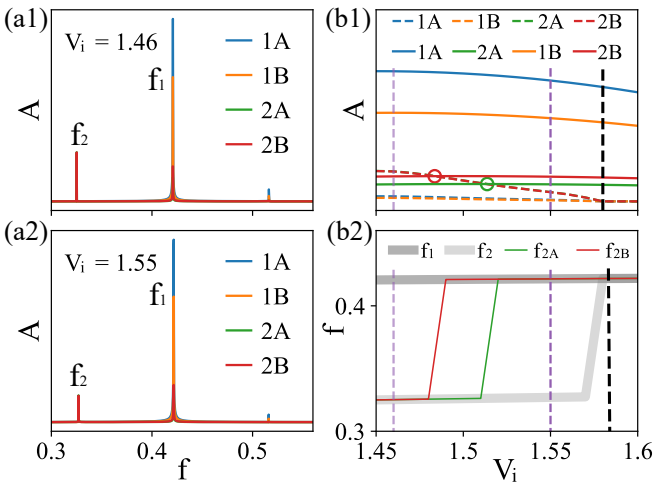


FIG. 7. (a1, a2) The Fourier spectrum of two parameter points in the CTQC phase of 2DAF mode. (b1) The variation of the second largest amplitude and largest amplitude on each site. The intersections of dashed and solid lines with the same color are marked by circles of the corresponding color. Note the green dashed line are covered by the red dashed line. (b2) The variation of the dominant frequencies. Here, f_{1A} and f_{1B} always equals to f_1. By contrast, in this parameter region, f_{2A} and f_{2B} no longer always equal to f_2. The colored dashed lines represent the parameter choice in (a). The black line denotes the transition point at $V_{i,c} = 1.58$, where f_2 merges with f_1, which indicates that no obvious peak structure can be resolved near the frequency f_2.

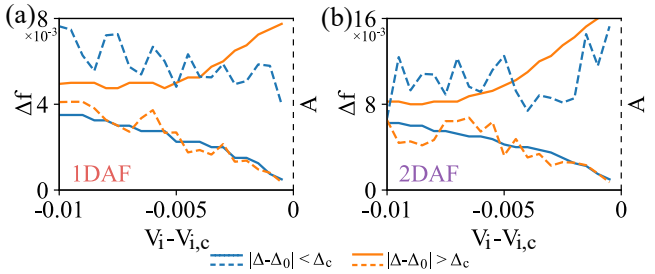


FIG. 8. The secondary frequency f_2 and its corresponding amplitude in the CTQC phase for the 1DAF mode in (a) and the 2DAF mode in (b). The blue and yellow curves correspond to parameter choices of $|\Delta - \Delta_0|$ associated with saddle-node and torus bifurcations, respectively. The solid and dashed lines denote the frequency difference Δf and relative amplitude $A(f_2)$, respectively.Owing to the finite frequency resolution, the solid curves exhibit a step-like structure. In addition, the amplitude varies non-smoothly with the control parameter because it is extracted from a discrete Fourier transform. The parameter values are $|\Delta - \Delta_0| = 0.18$ for the saddle-node bifurcation and 0.19 for the torus bifurcation in (a). In (b), $|\Delta - \Delta_0| = 0.49$ and 0.5 for two bifurcations, respectively. The data are obtained from the time-dependent dynamics evaluated at the 1A site, with an effective simulation time of 5×10^4.

boundary and phase region for two synchronization modes. The 2DAF mode exhibits CTQC, and CTC phases, whose boundaries are separated by pink data points; By contrast, the 1DAF mode shows CTQC, CTC and the steady state (SS) phases, separated by the red and yellow data points, respectively. As for the oscillatory solution of the 1DAF mode, it exists only at small inter-chain interaction strength $V_i \lesssim 1.5$, while for the 2D mode, it extends across the entire interaction range. The reason is that, as an emergent synchronization mode due to the inhomogeneous interaction strength in two directions [46], the 1DAF synchronization mode is easily affected by the asymmetry between the inter-chain and intra-chain interaction. When the asymmetry decreases, e.g. V_i closed to V, the CTQC transfers to CTC phase, and steady state (SS) in sequence, and finally disappears, leaving only the 2DAF mode. Due to the mismatch of the two boundaries, there are a total of six phases in the current phase diagram. In particular, we numerically show the solution of the phase with one quasi-periodic oscillatory mode, coexistent with the other periodic oscillatory mode [Fig. 6(b) and (c)].

In spite of the smoothness and simplicity of the 2DAF mode phase boundary, a noticeable issue is that, as the distance between two parameter points increases, the system needs more coupling to reach the CTC phase at the very beginning. However, for a larger frequency difference, e.g. $|\Delta - \Delta_0| \gtrsim 0.8$, the transition point moves to smaller V_i. The behavior demonstrates a different mechanism to the evolution from CTQC to CTC, illustrated by the evolution of the Fourier spectrum near the transition point shown by the black array in Fig. 6. We plot the single site Fourier spectrum in CTQC phase [Fig. 7(a)], the significant difference with the transition behavior above is that Δf does not approach zero, but the amplitude of the second dominant Fourier component gradually goes to zero. To clearly indicate this, we show the variation of the dominant frequencies and their associated amplitudes [Fig. 7(b)]. Here, the dashed (solid) curves in Fig. 7(b1) represent the second largest (largest) Fourier spectrum of each site. In particular for $2B$ sites labeled by red, the dashed curve crosses with the solid curve. According to the definition, f_{2B} will have an abrupt jump to merge with f_1 in Fig. 7(b2), at the position marked by the red circle in Fig. 7(b1). Finally, $A(f \neq f_2)$ vanishes and the CTC behavior appears with a single main frequency, indicated by the black dashed line. Therefore, at a large initial frequency difference, the frequency relation of near transition point Eq. (5) is replaced by an approximately constant dependency relationship. We therefore conclude that this transition is driven by the gradual suppression of the amplitude of the second characteristic frequency, and is more consistent with a torus bifurcation scenario. This mechanism is qualitatively distinct from the first type of transition with saddle-node bifurcation, indicating that the two transitions originate from fundamentally different dynamical structures.

An intriguing question is whether the transition between the two bifurcation mechanisms is abrupt or continuous. To address this issue, we fix several values of $|\Delta - \Delta_0|$, scan the interaction strength, and identify the underlying bifurcation mechanism by tracking both the position of the secondary frequency f_2, and its spectral amplitude $A(f_2)$. Figure 8 presents the corresponding results for both the 1DAF and 2DAF modes as the system approaches $V_{i,c}$ from the CTQC phase. In par-

ticular, we select two nearby values of $|\Delta - \Delta_0|$, separated by only 0.01, which are represented by the blue and yellow curves. For the blue curves, the frequency difference Δf continuously approaches zero while $A(f_2)$ remains finite, which is characteristic of the frequency-locking scenario described by the saddle-node bifurcation. In contrast, for the yellow curves, $A(f_2)$ vanishes while Δf remains finite, consistent with a torus-bifurcation scenario driven by the collapse of the secondary oscillation amplitude. These results indicate that the crossover between the two bifurcation mechanisms is confined to a parameter window narrower than 0.01, suggesting an effectively sharp transition within our numerical resolution. At the putative transition point, denoted by $|\Delta - \Delta_0| = \Delta_c$, it is natural to expect that both Δf and $A(f_2)$ simultaneously vanish. Such a simultaneous occurrence of frequency locking and amplitude collapse may signal a codimension-2 bifurcation point in the higher-dimensional parameter space.

VI. SUMMARY AND OUTLOOK

We investigate the dynamical behavior of two coupled Rydberg atomic chains with distinct intrinsic oscillation frequencies. By constructing the corresponding MF phase diagram, we reveal a rich structure that includes coexisting quasi-periodic oscillations described by two different synchronization regimes. The results obtained from various complementary approaches, such as Fourier spectral analysis, Poincaré sections, Lyapunov exponents, and phase-space trajectories, are mutually consistent.

From the perspective of synchronization, the quasi-periodic oscillations can be interpreted as a partially synchronized regime. Within the specific model and treatment considered here, this phase is stable and does not evolve into the chaotic behavior that is often expected. Notably, this work examines the synchronization between two oscillators under coherent coupling, and discovers two different regimes. When the initial frequency mismatch is small, the dominant frequencies of the two oscillators gradually approach each other, and their difference decreases with a square-root dependence on the tuning parameter. In contrast, when the initial frequency mismatch is large, the frequency difference remains nearly constant as the system approaches the phase transition point, while the relative weights of different frequency components are redistributed.

Looking ahead, this line of research can be extended in several directions. On the one hand, one may explore whether specific systems support novel synchronization patterns, such as those involving multiple subsystems. On the other hand, it is of interest to investigate the effects of different coupling mechanisms, for instance dissipative coupling, on the resulting dynamics. In summary, our results provide both a theoretical and experimentally feasible route to a novel dynamical phase-a CTQC, and offer a concrete paradigm for studying synchronization phenomena.

VII. ACKNOWLEDGMENT

This work is supported by National Natural Science Foundation of China (Project Nos. U25A20198 and 12404275), and the Fundamental Research Program of Shanxi province (Project No. 202403021212015).

APPENDIX A: DERIVATION ON THE EQUATION OF MOTION

In this section, we briefly present the mean-field (MF) treatment of the Hamiltonian in Eq. (1) of the main text. The evolution of an observable $\hat{O}$ follows

$$\begin{aligned} \partial_t\langle O\rangle &= -i\langle[H,O]\rangle + \langle\mathcal{L}(O)\rangle \\ \mathcal{L}(O) &= \gamma\sum_i\left(\sigma_i^- O\sigma_i^+ - \frac{1}{2}\{n_i,O\}\right). \end{aligned} \tag{6}$$

Where $\langle\cdots\rangle$ denotes expectation values. Within the first order MF approach, we consider the diagonal matrix element n_i and the non-diagonal matrix element σ_i as the dominant observables. Bringing them into Eq. (6), the commutator with the interaction term H_{int} gives $\langle n_i\sigma_j^-\rangle$. In particular, on account of the nearest-neighbor (NN) interaction and the next-nearest neighbor (NNN) interaction, the explicit formula $[H_{\text{int}},\sigma_{1,i}^-]$ writes (site on chain 1 for example),

$$\sigma_{1,i}^-(Vn_{1,i-1}+Vn_{1,i+1}+V_in_{2,i}+V_{i2}n_{2,i-1}+V_{i2}n_{2,i+1}\cdots) \tag{7}$$

Next we adopt the MF approximation $\langle AB\rangle \approx \langle A\rangle\langle B\rangle$ to average value of the first-order observables, denoted as first order MF approach. Under such approximation, the group of observables constitutes a closed form and can be directly solved numerically. Beyond that, considering the translation symmetry of the solution, we choose four site regions as the repeated unit, i.e. denoting $n_I = \langle n_i\rangle$ and $\sigma_I = \langle\sigma_i^-\rangle$, where $I \in$ 1A, 1B, 2A, 2B, and i belongs to the any sites on the whole two-chain model. Then the final equation of motion (EOM) of the two chains transfer to the eight coupled differential equations,

$$
\begin{aligned}
&\partial_t n_{1\mathrm{A}} = \Omega_1 \mathrm{Im}\sigma_{1\mathrm{A}} - \gamma n_{1\mathrm{A}}, \quad \partial_t \sigma_{1\mathrm{A}} = -\frac{\gamma}{2}\sigma_{1\mathrm{A}} - i(\Delta_1 - 2Vn_{1\mathrm{B}} - V_i n_{2\mathrm{A}} - 2V_{i2} n_{2\mathrm{B}})\sigma_{1\mathrm{A}} - i\frac{\Omega_1}{2}(2n_{1\mathrm{A}} - 1) \\
&\partial_t n_{1\mathrm{B}} = \Omega_1 \mathrm{Im}\sigma_{1\mathrm{B}} - \gamma n_{1\mathrm{B}}, \quad \partial_t \sigma_{1\mathrm{B}} = -\frac{\gamma}{2}\sigma_{1\mathrm{B}} - i(\Delta_1 - 2Vn_{1\mathrm{A}} - V_i n_{2\mathrm{B}} - 2V_{i2} n_{2\mathrm{A}})\sigma_{1\mathrm{B}} - i\frac{\Omega_1}{2}(2n_{1\mathrm{B}} - 1) \\
&\partial_t n_{2\mathrm{A}} = \Omega_2 \mathrm{Im}\sigma_{2\mathrm{A}} - \gamma n_{2\mathrm{A}}, \quad \partial_t \sigma_{2\mathrm{A}} = -\frac{\gamma}{2}\sigma_{2\mathrm{A}} - i(\Delta_2 - 2Vn_{2\mathrm{B}} - V_i n_{1\mathrm{A}} - 2V_{i2} n_{1\mathrm{B}})\sigma_{2\mathrm{A}} - i\frac{\Omega_2}{2}(2n_{2\mathrm{A}} - 1) \\
&\partial_t n_{2\mathrm{B}} = \Omega_2 \mathrm{Im}\sigma_{2\mathrm{B}} - \gamma n_{2\mathrm{B}}, \quad \partial_t \sigma_{2\mathrm{B}} = -\frac{\gamma}{2}\sigma_{2\mathrm{B}} - i(\Delta_2 - 2Vn_{2\mathrm{A}} - V_i n_{1\mathrm{B}} - 2V_{i2} n_{1\mathrm{A}})\sigma_{2\mathrm{B}} - i\frac{\Omega_2}{2}(2n_{2\mathrm{B}} - 1).
\end{aligned} \tag{8}
$$

Notice that Rydberg population n is always a real number, while σ is a complex number. Therefore, in the real calculation, there are totally 12 variables, which means the dimension of phase space is 12-dimension, and there exists 12 eigenvalues in Lyapunov exponent calculation.

To verify the robustness of the CTQC phase, we also consider the high-order non-linear term within the first order MF approach. It is reported in [47], that the term $\langle n\rangle^\beta\langle\sigma\rangle$ in EOM has a very significant impact on the emergence of the periodic solution in three-level system, where β is an integer exponent. Physically, such a term originates from the dynamics of the previous mentioned term $\langle n_i\sigma_j\rangle$. Concretely, it has its own dynamics if one does not perform the MF approach, and will return $\langle n_i^2\sigma_j\rangle$ in the commutator $[n_i\sigma_j, H_{\mathrm{int}}]$. This process will continue to generate $\langle n\rangle^\beta\langle\sigma\rangle$ for large β, unless one uses MF approximation to truncate a finite number of coupled equations, and omit the dynamics of the high-order operators. Therefore, without loss of generality, we could direct add nonlinearity to Eq.(8) to the first order MF approximation,

$$
\sum_J \sigma_I(V_{IJ}n_J + V_{IJ,2}n_J^2 + \cdots) \tag{9}
$$

where V_{IJ} is the interaction coefficient between site I, J after MF approximation. Here we only consider $\beta = 2$ as high-order correction, and denote $V_{IJ,2} = rV_{IJ}$, where r serves the only tuning parameter. The case for $r = 0$ goes back to the original first-order MF approximation.

[1] Weimer H, Müller M, Lesanovsky I, Zoller P and Büchler H P 2010 Nature Physics **6** 382–388 ISSN 1745-2481 URL https://doi.org/10.1038/nphys1614

[2] Labuhn H, Barredo D, Ravets S, de Léséleuc S, Macrì T, Lahaye T and Browaeys A 2016 Nature **534** 667–670 ISSN 1476-4687 URL https://doi.org/10.1038/nature18274

[3] de Léséleuc S, Lienhard V, Scholl P, Barredo D, Weber S, Lang N, Büchler H P, Lahaye T and Browaeys A 2019 Science **365** 775–780 URL https://www.science.org/doi/abs/10.1126/science.aav9105

[4] Keesling A, Omran A, Levine H, Bernien H, Pichler H, Choi S, Samajdar R, Schwartz S, Silvi P, Sachdev S, Zoller P, Endres M, Greiner M, Vuletić V and Lukin M D 2019 Nature **568** 207–211 ISSN 1476-4687 URL https://doi.org/10.1038/s41586-019-1070-1

[5] Samajdar R, Ho W W, Pichler H, Lukin M D and Sachdev S 2021 Proceedings of the National Academy of Sciences **118** e2015785118 URL https://www.pnas.org/doi/abs/10.1073/pnas.2015785118

[6] Bernien H, Schwartz S, Keesling A, Levine H, Omran A, Pichler H, Choi S, Zibrov A S, Endres M, Greiner M, Vuletić V and Lukin M D 2017 Nature **551** 579–584 ISSN 0028-0836, 1476-4687

[7] Bluvstein D, Omran A, Levine H, Keesling A, Semeghini G, Ebadi S, Wang T T, Michailidis A A, Maskara N, Ho W W, Choi S, Serbyn M, Greiner M, Vuletić V and Lukin M D 2021 Science **371** 1355–1359 ISSN 0036-8075, 1095-9203

[8] Bluvstein D, Levine H, Semeghini G, Wang T T, Ebadi S, Kalinowski M, Keesling A, Maskara N, Pichler H, Greiner M, Vuletić V and Lukin M D 2022 Nature **604** 451–456 ISSN 0028-0836, 1476-4687

[9] Bornet G, Emperauger G, Chen C, Ye B, Block M, Bintz M, Boyd J A, Barredo D, Comparin T, Mezzacapo F, Roscilde T, Lahaye T, Yao N Y and Browaeys A 2023 Nature **621** 728–733 ISSN 0028-0836, 1476-4687

[10] González-Cuadra D, Hamdan M, Zache T V, Braverman B, Kornjača M, Lukin A, Cantú S H, Liu F, Wang S T, Keesling A, Lukin M D, Zoller P and Bylinskii A 2025 Nature **642** 321–326 ISSN 1476-4687 URL https://doi.org/10.1038/s41586-025-09051-6

[11] Chen C, Bornet G, Bintz M, Emperauger G, Leclerc L, Liu V S, Scholl P, Barredo D, Hauschild J, Chatterjee S, Schuler M, Läuchli A M, Zaletel M P, Lahaye T, Yao N Y and Browaeys A 2023 Nature **616** 691–695 ISSN 0028-0836, 1476-4687

[12] Chen C, Emperauger G, Bornet G, Caleca F, Gély B, Bintz M, Chatterjee S, Liu V, Barredo D, Yao N Y, Lahaye T, Mezzacapo F, Roscilde T and Browaeys A 2025 Science **389** 483–487 URL https://www.science.org/doi/abs/10.1126/science.adn0618

[13] De Léséleuc S, Lienhard V, Scholl P, Barredo D, Weber S, Lang N, Büchler H P, Lahaye T and Browaeys A 2019 Science **365** 775–780 ISSN 0036-8075, 1095-9203

[14] Labuhn H, Barredo D, Ravets S, De Léséleuc S, Macrì T, Lahaye T and Browaeys A 2016 Nature **534** 667–670 ISSN 0028-0836, 1476-4687

[15] Ebadi S, Keesling A, Cain M, Wang T T, Levine H, Bluvstein D, Semeghini G, Omran A, Liu J G, Samajdar R, Luo X Z, Nash B, Gao X, Barak B, Farhi E, Sachdev S, Gemelke N, Zhou L, Choi S, Pichler H, Wang S T, Greiner M, Vuletić V and Lukin M D 2022 Science **376** 1209–1215 URL https://www.science.org/doi/abs/10.1126/science.abo6587

[16] Ebadi S, Wang T T, Levine H, Keesling A, Semeghini G, Omran A, Bluvstein D, Samajdar R, Pichler H, Ho W W, Choi S, Sachdev S, Greiner M, Vuletić V and Lukin M D 2021 Nature **595** 227–232 ISSN 0028-0836, 1476-4687

[17] Ferioli G, Glicenstein A, Ferrier-Barbut I and Browaeys A 2023 Nature Physics **19** 1345–1349 ISSN 1745-2473, 1745-2481

[18] Liang Q Y, Venkatramani A V, Cantu S H, Nicholson T L, Gullans M J, Gorshkov A V, Thompson J D, Chin C, Lukin M D and Vuletić V 2018 Science **359** 783–786 ISSN 0036-8075, 1095-9203

[19] Manovitz T, Li S H, Ebadi S, Samajdar R, Geim A A, Evered S J, Bluvstein D, Zhou H, Koyluoglu N U, Feldmeier J, Dolgirev P E, Maskara N, Kalinowski M, Sachdev S, Huse D A, Greiner M, Vuletić V and Lukin M D 2025 Nature **638** 86–92 ISSN 0028-0836, 1476-4687

[20] Maskara N, Ostermann S, Shee J, Kalinowski M, McClain Gomez A, Araiza Bravo R, Wang D S, Krylov A I, Yao N Y, Head-Gordon M, Lukin M D and Yelin S F 2025 Nature Physics **21** 289–297 ISSN 1745-2481 URL https://doi.org/10.1038/s41567-024-02738-z

[21] Omran A, Levine H, Keesling A, Semeghini G, Wang T T, Ebadi S, Bernien H, Zibrov A S, Pichler H, Choi S, Cui J, Rossignolo M, Rembold P, Montangero S, Calarco T, Endres M, Greiner M, Vuletić V and Lukin M D 2019 Science **365** 570–574 ISSN 0036-8075, 1095-9203

[22] Qiao M, Emperauger G, Chen C, Homeier L, Hollerith S, Bornet G, Martin R, Gély B, Klein L, Barredo D, Geier S, Chiu N C, Grusdt F, Bohrdt A, Lahaye T and Browaeys A 2025 Nature ISSN 0028-0836, 1476-4687

[23] Scholl P, Schuler M, Williams H J, Eberharter A A, Barredo D, Schymik K N, Lienhard V, Henry L P, Lang T C, Lahaye T, Läuchli A M and Browaeys A 2021 Nature **595** 233–238 ISSN 0028-0836, 1476-4687

[24] Semeghini G, Levine H, Keesling A, Ebadi S, Wang T T, Bluvstein D, Verresen R, Pichler H, Kalinowski M, Samajdar R, Omran A, Sachdev S, Vishwanath A, Greiner M, Vuletić V and Lukin M D 2021 Science **374** 1242–1247 URL https://www.science.org/doi/abs/10.1126/science.abi8794

[25] Browaeys A and Lahaye T 2020 Nature Physics **16** 132–142 ISSN 1745-2481 URL https://doi.org/10.1038/s41567-019-0733-z

[26] Nguyen T L, Raimond J M, Sayrin C, Cortiñas R, Cantat-Moltrecht T, Assemat F, Dotsenko I, Gleyzes S, Haroche S, Roux G, Jolicoeur T and Brune M 2018 Phys. Rev. X **8**(1) 011032 URL https://link.aps.org/doi/10.1103/PhysRevX.8.011032

[27] Wilczek F 2012 Phys. Rev. Lett. **109**(16) 160401 URL https://link.aps.org/doi/10.1103/PhysRevLett.109.160401

[28] Zaletel M P, Lukin M, Monroe C, Nayak C, Wilczek F and Yao N Y 2023 Review of Modern Physics **95**(3) 031001 URL https://link.aps.org/doi/10.1103/RevModPhys.95.031001

[29] Kyprianidis A, Machado F, Morong W, Becker P, Collins K S, Else D V, Feng L, Hess P W, Nayak C, Pagano G, Yao N Y and Monroe C 2021 Science **372** 1192–1196 ISSN 0036-8075, 1095-9203

[30] Keßler H, Kongkhambut P, Georges C, Mathey L, Cosme J G and Hemmerich A 2021 Physical Review Letters **127** 043602 ISSN 0031-9007, 1079-7114

[31] Iemini F, Russomanno A, Keeling J, Schirò M, Dalmonte M and Fazio R 2018 Physical Review Letters **121** 035301 ISSN 0031-9007, 1079-7114

[32] Yao N Y, Nayak C, Balents L and Zaletel M P 2020 Nature Physics **16** 438–447 ISSN 1745-2481 URL https://doi.org/10.1038/s41567-019-0782-3

[33] Strogatz S H 2001 Nonlinear Dynamics and Chaos (Westview Press)

[34] Wu X, Wang Z, Yang F, Gao R, Liang C, Tey M K, Li X, Pohl T and You L 2024 Nature Physics **20** 1389–1394 ISSN 1745-2481 URL https://doi.org/10.1038/s41567-024-02542-9

[35] Liu B, Zhang L H, Wang Q F, Ma Y, Han T Y, Zhang J, Zhang Z Y, Shao S Y, Li Q, Chen H C, Shi B S and Ding D S 2024 Nature Communications **15** 9730 ISSN 2041-1723 URL https://doi.org/10.1038/s41467-024-53712-5

[36] Liu B, Zhang L H, Ma Y, Wang Q F, Han T Y, Zhang J, Zhang Z Y, Shao S Y, Li Q, Chen H C, Guo G C, Ding D S and Shi B S 2025 Nature Communications **16** 1419 ISSN 2041-1723 URL https://doi.org/10.1038/s41467-025-56712-1

[37] Sacha K 2022 Reports on Progress in Physics **85** 096001

[38] Huang Y, Wang T, Yin H, Jiang M, Luo Z and Peng X 2025 Nature Communications **16** 9375 ISSN 2041-1723 URL https://doi.org/10.1038/s41467-025-64413-y

[39] Solanki P and Minganti F 2025 Phys. Rev. B **112**(13) 134311 URL https://link.aps.org/doi/10.1103/b6gq-z5nf

[40] Flicker F 2017 SciPost Physics **3** 020 (*Preprint* 1707.09371)

[41] Boyle L and Mygdalas S 2026 (*Preprint* 2601.07769) URL https://arxiv.org/abs/2601.07769

[42] He G, Ye B, Gong R, Yao C, Liu Z, Murch K W, Yao N Y and Zu C 2025 Phys. Rev. X **15**(1) 011055 URL https://link.aps.org/doi/10.1103/PhysRevX.15.011055

[43] Luo X, Zhou Y, Xu Z and Jiang W 2026 Communications Physics ISSN 2399-3650 URL https://doi.org/10.1038/s42005-026-02572-0

[44] Feng X, Liu S, Chen S and Zhang S X 2025 (*Preprint* 2512.10303) URL https://arxiv.org/abs/2512.10303

[45] Lee T E, Häffner H and Cross M C 2011 Phys. Rev. A **84**(3) 031402 URL https://link.aps.org/doi/10.1103/PhysRevA.84.031402

[46] Jiang W 2025 Phys. Rev. A **112**(5) 052811 URL https://link.aps.org/doi/10.1103/87jf-zj5g

[47] Wadenpfuhl K and Adams C S 2023 Phys. Rev. Lett. **131**(14) 143002 URL https://link.aps.org/doi/10.1103/PhysRevLett.131.143002